Magnetic phase dependency of the thermal conductivity of FeRh from thermoreflectance experiments and numerical simulations

Aloïs Castellano, Kévin Alhada-Lahbabi, Jon Ander Arregi, Vojtěch Uhlíř, Bernard Perrin, Catherine Gourdon, Daniele Fournier, Matthieu Jean Verstraete, L. Thevenard

Magnetic phase dependency of the thermal conductivity of FeRh from thermoreflectance experiments and numerical simulations

A. Castellano,[1] K. Alhada-Lahbabi,[2] J. A. Arregi,[3] V. Uhlíř,[3,4] B. Perrin,[2]
C. Gourdon,[2] D. Fournier,[2] M. J. Verstraete,[1,5] and L. Thevenard[2]

[1]*NanoMat/Q-Mat Université de Liège, and European Theoretical Spectroscopy Facility, B-4000 Liège, Belgium*
[2]*Sorbonne Université, CNRS, Institut des Nanosciences de Paris, 4 place Jussieu, 75252 Paris, France*
[3]*CEITEC BUT, Brno University of Technology, Purkyňova 123, 612 00 Brno, Czech Republic*
[4]*Institute of Physical Engineering, Brno University of Technology, Technická 2, 616 69 Brno, Czech Republic*
[5]*ITP, Physics Department, Utrecht University 3508 TA Utrecht, The Netherlands*
(*thevenard@insp.jussieu.fr)

(Dated: April 3, 2024)

FeRh is well known in its bulk form for a temperature-driven antiferromagnetic (AF) to ferromagnetic (FM) transition near room temperature. It has aroused renewed interest in thin film form, with particular focus on its biaxial AF magnetic anisotropy which could serve for data encoding, and the possibility to investigate laser-assisted phase transitions, with varying contributions from electrons, phonons and magnons. In order to estimate the typical temperature increase occurring in these experiments, we performed modulated thermoreflectance microscopy to determine the thermal conductivity κ of FeRh. As often occurs upon alloying, and despite the good crystallinity of the layer, κ was found to be lower than the thermal conductivities of its constituting elements. More unexpectedly given the electrically more conducting nature of the FM phase, it turned out to be three times lower in the FM phase compared to the AF phase. This trend was confirmed by examining the temporal decay of incoherent phonons generated by a pulsed laser in both phases. To elucidate these results, first and second principles simulations were performed to estimate the phonon, magnon and electron contributions to the thermal conductivity. They were found to be of the same order of magnitude, and to give a quantitative rendering of the experimentally observed κ_{AF}. In the FM phase however, simulations overestimate the low experimental values, implying very different (shorter) electron and magnon lifetimes.

INTRODUCTION

The FeRh alloy near equiatomic composition is a unique magnetic material, studied long ago in bulk form[1,2], and which has recently sparked a renewed interest in thin film form for technological applications. The first-order metamagnetic phase transition of FeRh from the antiferromagnetic (AF) to the ferromagnetic (FM) state happens close to room temperature, and the associated changes in magnetic, electrical and thermodynamical properties have been utilized to propose novel approaches for memory cells[3], heat-assisted magnetic recording[4], and magnetic refrigeration[5]. FeRh thin films are also good candidates to investigate laser-assisted transient[6–12] or irreversible[13] phase transitions.

Excitation of the AF phase by a femtosecond laser pulse generates an out-of-equilibrium population of electrons and then phonons, whose temperatures eventually equilibrate, typically on picosecond time scales. The respective roles of electrons and phonons at the onset of a transient FM state are still much debated[7,8,10,11,14]. After this initial step on the ps timescale the local temperature decreases through heat diffusion. This evolution determines the nucleation, expansion and coalescence of FM domains as well as the decay of the transient magnetic moment upon cooling back to the AF phase[12]. However, the heat diffusion coefficient D of FeRh is poorly known. It is related to the thermal conductivity κ by $D = \kappa/(\rho C)$ where ρ is the mass density and C the specific heat. Both ρ and C are known to vary with temperature and magnetic phase[15,16]. The heat conductivity also determines the stationary temperature rise of the sample when the pulsed laser repetition rate is too high for the system to relax back to its base temperature between pulses[6,8,17–19], or when a CW laser or current is used to induce a local nucleation of FM domains[13,20]. Whereas specific heat measurements are reported for FeRh bulk[1,2,21] and thin film samples[16], the thermal conductivity is usually estimated from the electrical conductivity σ using the Wiedemann-Franz law $\kappa_e = L_0 T \sigma$, with L_0 being the Lorenz number[7]. A noteworthy exception is a recent paper by Ahn *et al.*[19] in which they evaluate indirectly κ_{AF}=11.8 and κ_{FM}=22.4 $\mathrm{W\,m^{-1}\,K^{-1}}$.

There are numerous reports of the material's electronic and phononic band structures, some expliciting calculations of its thermal properties[22–27]. Since FeRh is metallic, one could expect the electronic contribution to the thermal conductivity κ_e to be dominant over the phononic and magnonic (κ_{ph}, κ_m) ones, and to govern how κ should scale between its two magnetic phases. Relating in first approximation κ_e to the electrical conductivity using the Wiedemann-Franz law mentioned above gives a value almost twice larger in the FM phase as in the AF phase[28]. As for the phononic contribution, recent DFT calculations by Cazorla *et al.*[26] predict it to be very slightly smaller in the AF than the FM phase. Finally, there is no record yet – either experimental or numerical – for the magnonic contribution κ_m. In pure BCC Fe it has been estimated to represent about 10% of the total thermal conductivity[29]. Overall, calculations so far suggest the FeRh FM phase to be thermally more conductive than the AF one.

In this paper we determine the total thermal conductivity of a 195 nm FeRh thin film, using modulated thermoreflectance (TR) microscopy. It is an ideal technique to measure the thermal properties of thin films deposited on a substrate, when

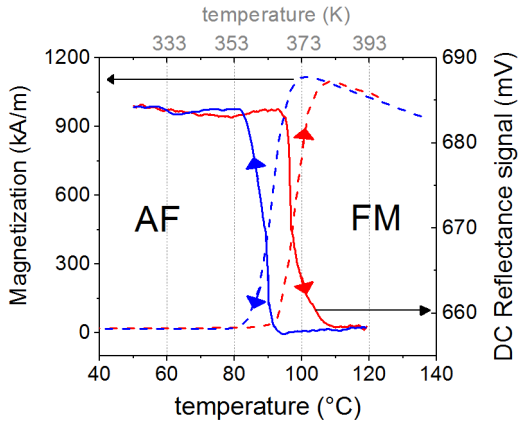

FIG. 1. Determination of the transition temperature of the film. Left: Global measurement of magnetization using vibrating sample magnetometry (dashed line). Right: Local measurement of the DC reflectance (continuous line) under probe beam only ($\lambda = 488$ nm, 0.8 µm spatial resolution) with a temperature ramp of 2 K/min.

the volume is too small to be probed by standard calorimetry techniques[30–33]. This enables us to estimate quantitatively transient and stationary laser-driven temperature rises. We confirm the results on thermal conductivity by monitoring the time decay of interferometric measurements in a pump-probe setup in both AF and FM phases. In parallel, we compute the electronic, magnetic and vibrational properties of the material, and the different contributions to the thermal conductivity in both phases. We then discuss how the total value compares to our data.

SAMPLE

An FeRh film with a thickness of $h = 195$ nm was deposited on a 500-µm-thick MgO(001) substrate via magnetron sputtering of an equiatomic FeRh target. The film was grown at 430°C after preheating the substrate for 60 min at the same temperature. We used an Ar pressure of 2.7×10^{-3} mbar and a sputtering power of 50 W, leading to a deposition rate of 2 nm min^{-1}. Post-growth annealing in high vacuum at 780°C for 80 min yielded a good quality and homogeneous CsCl-type structure of the film[15]. It is nearly fully relaxed, with a +0.03% strain in the out-of-plane direction at room temperature. Finally, a 2-nm-thick Pt cap was grown after cooling the sample below 120°C, to protect the film from oxidation.

The temperature-dependent magnetization data of the film measured via vibrating sample magnetometry (VSM) (Fig. 1) show a heating transition from AF to FM state between 87 and 108°C (360 and 381 K), and a cooling transition between 100 and 80°C (373 and 353 K). The very weak residual ferromagnetic contribution in the AF phase (4% of the magnetization at 400 K) is a signature of the excellent quality of the sample. The AF-FM transition can also be monitored locally by reflectance microscopy at variable temperature. For this the sample is glued with thermal paste on the holder of a Linkam cryostat adapted to a microscopy set-up. As expected for FeRh[34–36], a 3–4% hysteretic change of the phase-dependent reflectance $R(T)$ is observed at the AF-FM transition (Fig. 1). The slight difference in shape and position of the transition compared to the curve measured by VSM reflects the much smaller probed volume (a few µm^2 wide, and about 10 nm deep) and the spatial variations of the magnetic properties.

MODULATED THERMOREFLECTANCE EXPERIMENTS: METHODOLOGY AND RESULTS

We now briefly describe the home-built thermoreflectance microscope that allows to access the thermal properties of the sample.

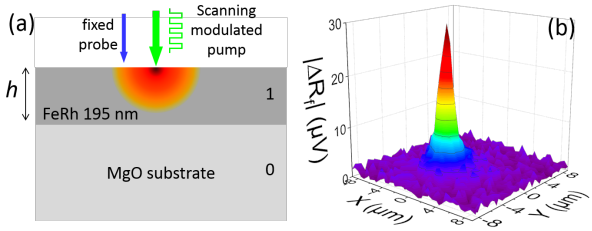

FIG. 2. (a) Schematics of the modulated thermoreflectance set-up. (b) 10×10 µm^2 map of the amplitude of the modulated thermoreflectance signal.

Light from a $\lambda = 488$ nm (blue) continuous wave (CW) laser (probe beam) is focused onto its surface to a diffraction-limited spot by a $\times50$ long-working-distance objective (numerical aperture NA = 0.5, working distance 10.6 mm). The typical power impinging on the sample is 120 µW. A heat source is provided by a 532 nm (green) CW laser passing through an acousto-optic modulator driven by a square modulation at frequency f and focused onto the sample by the objective (≈5.3 mW on the sample). This green laser spot is raster-scanned on the sample surface while the reflected blue probe beam is collected by the photodiode which monitors the reflectance of the layer. The green light reflected back towards the detector is blocked by an interference filter. The signal is fed into a lock-in amplifier that returns the amplitude and phase of the AC component of the reflectance at the frequency of the modulated heat source, ΔR_f, as well as the DC component R_0 thanks to an Analog to Digital Converter (ADC). A typical map of the modulated reflectance is shown in Fig. 2(b) (amplitude component).

As described in detail in Ref. 30, the reflectance is assumed to depend on the temperature increase to the first order $R(\mathbf{r},t)=R_0+\frac{\partial R_{probe}}{\partial T} I_{probe}(\mathbf{r}) * \Delta T(\mathbf{r},t)$, where the temperature profile is convolved with the probe spot profile $I_{probe}(\mathbf{r})$. The modulated reflectance ΔR_f at frequency f reflects the f-harmonic of the temperature increase ΔT_f induced by the pump laser. Modulation frequencies are moreover assumed to be low enough to consider the system at thermodynamic equilibrium, with the thermal flux being proportional to the tem-

perature gradient[30]. Adapting Ref. 37 and using cylindrical coordinates, the thermal field at the surface of the sample and the modulated reflectance are given by inverse Hankel transforms as detailed in Eqs. (1-3).

$$\Delta T_f(r) = \frac{Q_f}{2\pi}\int_0^\infty g(u)\,J_0(ur)\,u\exp\left(-\frac{d_{\text{pump}}^2u^2}{32}\right)du\,, \tag{1}$$

$$\Delta R_f(r) \propto \frac{\partial R_{probe}}{\partial T}\int_0^\infty g(u)\,J_0(ur)\,u\,A(u)\exp\left(-\frac{d_{\text{pump}}^2u^2}{32}\right)du\,, \tag{2}$$

$$g(u) = \frac{\alpha^2}{\alpha^2-\Sigma_1^2}\frac{\left(1-\frac{\kappa_0^*\Sigma_0}{\kappa_1\alpha}\right)\left(\cosh(\Sigma_1 h)-\exp(-\alpha h)\right)+\left(\frac{\kappa_0^*\Sigma_0}{\kappa_1\Sigma_1}-\frac{\Sigma_1}{\alpha}\right)\sinh(\Sigma_1 h)}{\kappa_0^*\Sigma_0\cosh(\Sigma_1 h)+\kappa_1\Sigma_1\sinh(\Sigma_1 h)}\,, \tag{3}$$

where $\Sigma_i(u,f)=\sqrt{u^2+j\frac{2\pi f}{D_i}}$ is akin to a complex thermal wave-vector ($j=\sqrt{-1}$). Indices 0 and 1 refer to the MgO substrate and the FeRh thin film, respectively. $D_i=\kappa_i/(\rho_i C_i)$ is the heat diffusivity with ρ_i and C_i the mass density and specific heat, respectively. $Q_f=\frac{4}{\pi}P_{inc}(1-R)$ is the f-component of the incoming modulated heat power with R the reflection coefficient at the pump wavelength. J_0 is the Bessel function of the first kind, and α is the absorption coefficient of the pump beam in FeRh[38]. The last two terms of Eq. (1) describe the finite diameter of the laser spots: $A(u)$ is the Hankel transform of the Airy pattern of the diffraction-limited probe spot, and d_{pump} is the diameter at which the intensity of the Gaussian pump spot has fallen by e^2. Numerical values for known parameters are given in Appendix A .

The temperature increase includes *all* contributions to the thermal conductivity: phononic, electronic, magnonic, as well as the effect of any thermal interface resistance (TIR) R_{th} between the substrate and the thin film due to a localized scattering of phonons. Taking into account the presence of a TIR amounts to using in Eq. (3) a modified thermal conductivity for the substrate $\kappa_0^*=\kappa_0/(1+R_{th}\kappa_0\Sigma_0)$[39]. We now discuss possible values to give to R_{th}. The TIR is notoriously complicated to measure reliably[40], particularly in the case of a thermally insulating film/conducting substrate configuration. It may have *intrinsic* origins such as *e.g.* Umklapp processes[41], or, more likely at play in our case, *extrinsic* origins such as interface roughness - expected to be minute in our epitaxial films. Applying the diffuse mismatch model to the FeRh/MgO interface yields $R_{th}\sim 4\times10^{-9}$ m^2 K W^{-1} for both magnetic phases (see below for numerical details on this simulation). This method is known to give a lower bound for thermal interface resistance, but matches reassuringly well with experimental values found in the literature for thin metallic films (e.g. Al or Cu) deposited on an electrically insulating substrate (e.g. SiO_2 or Al_2O_3)[42,43]. It is also quite close to the value (2×10^{-9} m^2 K W^{-1}) estimated indirectly for antiferromagnetic FeRh/MgO by Ahn *et al.*[19].

Modulated thermoreflectance spatial scans measured on FeRh/MgO are typical of a thermal insulator over conducting substrate configuration. In this case, heat diffuses rapidly to the substrate, and then back to the top layer. To illustrate this, we plot in Fig. 3(a) the amplitude of the temperature rise given by Eq. (2) at an example frequency of $f=250$ kHz, with and without an FeRh layer ($h=0$ or 195 nm). Far from the center, the behavior of the MgO substrate is recovered, with the slope essentially governed by the frequency-dependent thermal diffusion length $\mu_0=\sqrt{\frac{D_0}{\pi f}}$. The central temperature rise, on the other hand, roughly scales as $\frac{h}{\kappa_1}+R_{th}$ above the signal from the substrate (Fig. 3(a)). As a result, it is (i) quite challenging to measure reliably the thermal conductivity of very thin/highly conductive films, and justifies the use of a fairly thick (195 nm) film for this study, and (ii) almost impossible to determine independently R_{th} and κ_1, as the two terms always appear together[44]. To analyze our data, we thus chose to impose a value for R_{th} (see discussion above). Finally, we verified that the $r=0$ value of the amplitude scales linearly with the incident power.

TABLE I. Thermal conductivity extracted from group fits of the log of the amplitude of the modulated reflectivity, imposing $R_{th}=4\times10^{-9}$ m^{2}K W^{-1} as explained in the text.

Temperature (°C)	Phase	Thermal conductivity (W m^{-1} K^{-1})
5	AF	26 ±3
40	AF	30 ±5
60	AF	30 ±5
100	FM	10±1
130	FM	9 ±1

In order to evaluate the thermal conductivity of FeRh at a given temperature, we record spatial scans of the amplitude and phase of the modulated thermoreflectance signal at three modulation frequencies (typically 100, 250 and 500 kHz), as shown for instance for $T=100$°C (373 K) in Fig. 3(b)-(c). We then perform a global fit of the logarithm of the normalized amplitude of the three curves, with the thermal conductivity of FeRh being the only free (shared) parameter and the pump beam diameter and TIR imposed. Starting from an identical value of $R_{th}=4\times10^{-9}$ m^2 K W^{-1} in both AF and FM phases, we also explore the possibility of a much larger TIR in the FM phase, and use the quality of the fit to validate the chosen value. Note that no knowledge of $\frac{\partial R_{probe}}{\partial T}$ is necessary

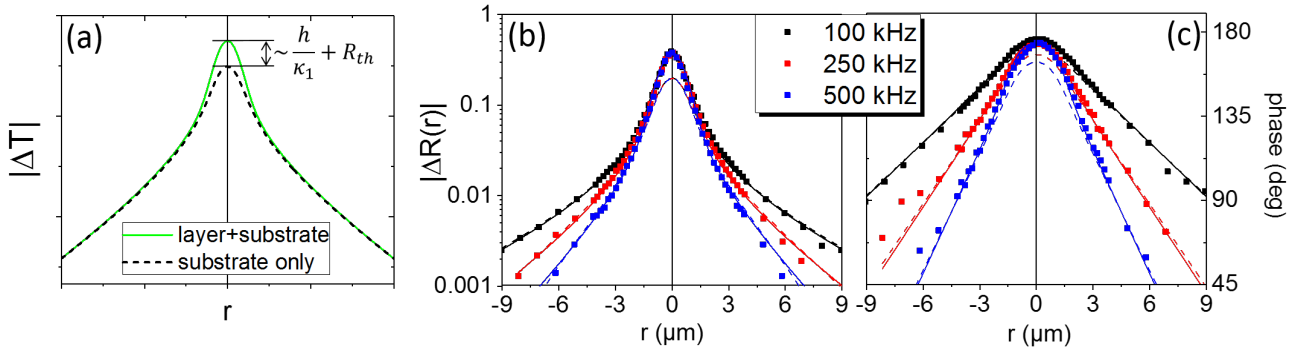

FIG. 3. (a) Illustration of the effect of the presence of a thin film over a better thermally conducting substrate : logarithm of the temperature rise induced by a 250 kHz modulated laser, with and without the 195-nm-thick FeRh film (Eq. 1) . The "nose" contains information on the layer's thermal conductivity and on the thermal interface resistance. (b-c) Experimental spatial scans of amplitude and phase taken at three modulation frequencies in the uniform FM phase (T = 100°C, 373 K). The fit of $\log|\Delta R|$ by Eq. (1) yields $\kappa_1 = 10\pm1$ W m^{-1} K^{-1}. The response of the FeRh/MgO system (full line) and MgO substrate only (dashed line) are plotted using d=2.1 μm and $R_{th} = 4\times10^{-9}$ m^{2}K W^{-1}.

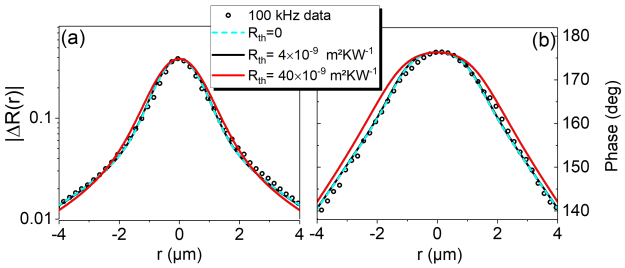

FIG. 4. (a) Amplitude and (b) phase at 100 kHz modulation frequency in uniform FM phase (T = 100°C, 373 K). Fitting the data with different thermal interface resistances R_{th}=0, 4 or 40 × 10^{-9} m^{2}K W^{-1} gives κ_1 = 9, 10 or 20 W m^{-1} K^{-1} (resp. green, blue and red curves). The amplitude and phase are then calculated with Eq.(2). Note that the difference between R_{th}=0 and 40 × 10^{-9} m^{2}K W^{-1} curves is minute, and that the agreement with the phase data is poor for the larger TIR.

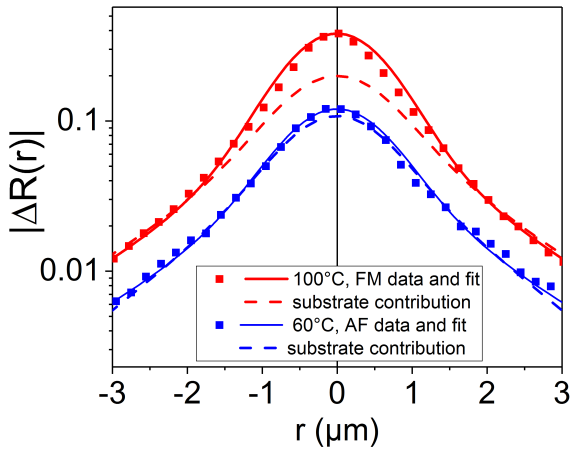

FIG. 5. Amplitude of the modulated reflectivity measured at 500 kHz in the uniform AF (resp. FM) phases at T=60°C in blue symbols (resp. T=100°C in red symbols). Full lines are fit to the data with κ_1=30 Wm^{-1}K^{-1} (AF) and κ_1=10 Wm^{-1}K^{-1} (FM), while the dashed line is the contribution of the MgO substrate.

to extract κ_1 from this analysis, since it is the relative spatial variations of the f-component of the reflectance that are of importance. Finally, complementary MatLab simulations including a third layer in the model confirm that we can neglect the presence of the thin Pt cap in the analysis of the data.

Table I shows the final temperature dependence of the thermal conductivity of the 195-nm-thick FeRh film, established using the group fit procedure described above. The overall trend is distinctly that of a smaller value of $\kappa_1(T)$ in the FM phase compared to the AF phase. More specifically, κ_1 is 25-30 W m^{-1} K^{-1} in the AF phase, and around 10 W m^{-1} K^{-1} in the FM phase, *i.e.*, almost three times less. This shows up clearly when plotting together spatial scans measured at the highest AF temperature (60°C) and lowest FM temperature (100°C), in Fig. 5. The "nose" of the AF spatial scan is strikingly smaller than in the FM scan. This could either be due to a smaller thermal conductivity in the FM phase, or to a much larger interface resistance. To test the latter hypothesis, we fit the FM data imposing a very large value of $R_{th} = 4\times10^{-8}$ m^2 K W^{-1} (red curve in Fig. 4). This does yield a higher $\kappa_{1,FM}$ of around 20 W m^{-1}K^{-1}, but at the cost of a poorer fit quality, particularly visible on the phase (Fig. 4(b)). Note that this method sets an *upper* boundary to a likely value for R_{th}, while DFT simulations give a lower limit.

We can now estimate the heat diffusivity $D_1 = \frac{\kappa_1}{\rho_1 C_1}$ of FeRh in both phases. Since the volume density of FeRh ρ_1 varies appreciably with the magnetic phase (AF or FM, see Appendix A for numerical values), D_1 is divided by over two upon crossing the transition: from $\sim 8\times10^{-6}$ m^2 s^{-1} in the AF phase at 5°C, to $\sim 3\times10^{-6}$ m^2 s^{-1} in the FM phase at 130°C (403 K). Note that the former value is in the range of the diffusivity of 2×10^{-5} m^2 s^{-1} found by Bergman *et al.*[8] by fitting the laser-induced transient reflectivity, late after the

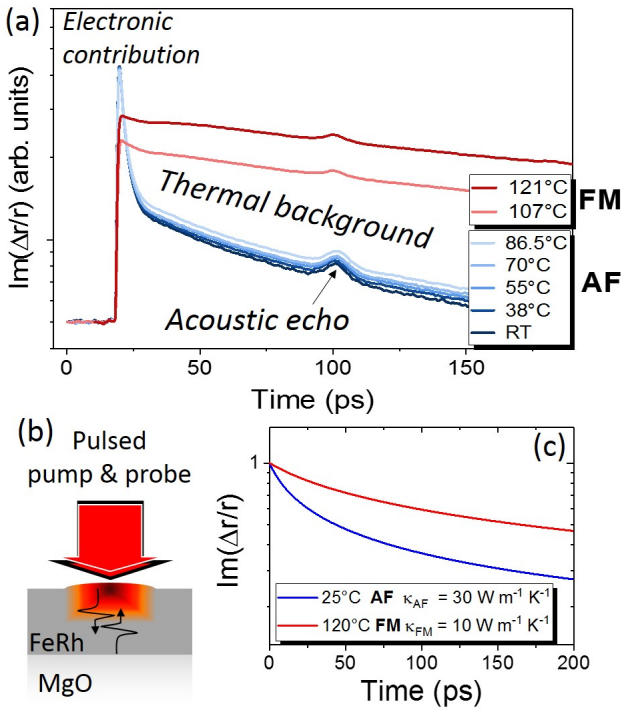

FIG. 6. (a) Interferometric signal at different temperatures on either side of the transition obtained using a time-resolved pump-probe setup (b)[45], with large diameter spots. Incoherent phonon generation occurs together with the launching of a thermo-elastically generated *coherent* strain wave that travels rapidly to the FeRh/MgO interface and back. The more rapid decay of the thermal background in the AF phase indicates a higher thermal conductivity as evidenced from (c) the calculated interferometric signal, given by Eq. 4 and normalized to its $t = 0$ value.

arrival of the pulse, when the layer is back into its AF phase. This makes FeRh roughly as heat-diffusive as MgO in its AF phase, but almost four times less in the FM phase. Typical thermal diffusion lengths at 500 kHz are then of a few microns, much more than the film thickness. A rough estimate in a 1D approximation moreover gives the typical time it takes for the heat to escape laterally a $d \approx 2$ µm diameter heat spot as $\tau \approx \frac{d^2}{D_1}$, i.e., $\tau_{\mathrm{AF}} \approx 500$ ns while $\tau_{\mathrm{FM}} \approx 1.2$ µs.

CONFIRMATION OF $\kappa_{AF} > \kappa_{FM}$ USING PULSED GENERATION OF INCOHERENT PHONONS

The analysis of the thermoreflectance data points to a smaller thermal conductivity in the FM phase compared to the AF phase, even considering a larger thermal interface resistance at high temperature. This comes as a surprising result given that both the Wiedeman-Franz law and a previous experimental estimate[19] seemed to indicate instead a larger thermal conductivity in the FM phase. To verify this, we performed picosecond acoustics pump-probe experiments (see Fig. 6, and Appendix B for experimental details). A 80 MHz femtosecond laser beam is split in a train of pump pulses that generate coherent strain waves by the thermoelastic effect, and delayed probe pulses that measure the dephasing of the reflected electric field of light by interferometry[45]. After an electronic signal decaying within 10-20 ps, one observes a slower decay related to the cooling of the layer as the heat is evacuated from the 12-13 nm thick top layer in which the light has been absorbed (Fig. 6(a)). It is clearly slower in the FM compared to the AF phase, as it is also observed in the time-resolved strain measurements by Ahn *et al.* in Ref. 19 (see in particular their Supplemental Information[46]). This indicates once more $\kappa_{1,AF} > \kappa_{1,FM}$. We can this time safely discard the influence of the interface resistance on the thermal background during the $t_{ps} = 300$ ps window of observation: whereas the longitudinal acoustic wave traveling at 4741 m s^{-1} easily sees the FeRh interface twice, the thermal wave will only have reached around $l_{th}=\sqrt{Dt_{ps}} \approx$ 30-50 nm deep into the FeRh layer. The interferometric signal is calculated as $\mathrm{Im}\left(\Delta r(t)/r\right)$ where r is the amplitude reflection coefficient of the light electric field (Eq. 4). The first term contains the surface displacement $u(t, z = 0)$. k_0 equal to $2\pi/\lambda$ is the light wavevector. The next term describes the reabsorption and dephasing of the reflected light taking into account the change of the refractive index $n = n' + jn''$ induced by the propagating strain pulse S_{prop} and the temperature variation ΔT arising from heat diffusion.

$$\frac{\Delta r(t)}{r} = 2jk_0 u(t, z = 0) + jk_0 \frac{4n}{(1-n^2)} \int_0^\infty \left(\frac{dn}{dS} S_{prop}(t, z) + \frac{dn}{dT} \Delta T(t, z) \right) \exp\left(j2k_0 nz\right) dz \tag{4}$$

The detailed expressions of $u(t, z = 0)$, $S_{prop}(t, z)$ and $\Delta T(t, z)$ and the parameters used in the modelling are given in Appendix B. The surface displacement and propagating strain are found to give smaller contributions to the interferometric signal as compared to heat diffusion. This signal is calculated using the thermal diffusivity given by κ values in Table I and shown in Fig. 6(c). It clearly evidences a faster decay in the AF phase with a larger diffusivity, in good agreement with the experimental results of Fig. 6(a).

DISCUSSION

Having confirmed the trend $\kappa_{1,AF} > \kappa_{1,FM}$ seen on the modulated thermoreflectance data, we compare the values of the thermal conductivity in both phases (Table I), with that of other materials at room temperature. The absolute values are overall smaller than for[47] good metals (a few hundreds W m^{-1} K^{-1}), semiconductors ($\approx$ 10–100 W m^{-1} K^{-1}), or even an electrical insulator such as MgO

(≈ 50 W m^{-1} K^{-1}). As often occurs upon alloying[48], the thermal conductivity of FeRh is also smaller than those of its constituting single elements[47,49]: $\kappa_{Fe} \approx 80$ W m^{-1} K^{-1} and $\kappa_{Rh} \approx 135$ W m^{-1} K^{-1}.

We can moreover estimate the stationary temperature increase due to the modulated green laser only, ΔT_{stat}, using Eq. (2) in which we set the frequency $f = 0$, r=0, and the incoming heat flow as $Q_0 = P_{inc}(1-R)$. For an incident average laser power of $P_{inc} \approx 5.3$ mW, the stationary temperature rise in the very center of a 2-µm-diameter pump spot will thus be of $\Delta T_{stat} \approx 13$ °C for a base temperature of 40 or 60 °C (313 or 333 K) in the AF phase ($\kappa_1 \approx 30$ W m^{-1} K^{-1}). Note that this estimate is strongly dependent on the probe spot diameter.

CALCULATIONS OF κ_e, κ_{ph}, κ_m AND R_{th}

To dissect the experimentally observed and counter-intuitive thermal conductivity of FeRh, we perform simulations and combine with literature data to understand the individual phonon, electron and magnon contributions for the FM and AF phases.

Phonon thermal conductivity: anharmonic phonon calculations

From an *ab initio* setting, the lattice contribution to the thermal conductivity can be computed by solving the phonon Boltzmann equation[50–52]. In order to obtain quantitative results, it is essential to include effects beyond the harmonic approximation, such as thermal expansion and intrinsic anharmonicity, in the description of the system. This seems to be particularly true for the AF phase of FeRh, where previous theoretical studies predicted the appearance of an imaginary mode[22,53–55], which prevents the use of the harmonic approximation as a starting point for the Boltzmann equation. To go beyond the harmonic approximation, we employ the temperature dependent effective potential (TDEP) method[52,56,57] to include anharmonicity and renormalize phonon-phonon interactions. To reduce the important simulation cost while keeping the accuracy of DFT, we constructed two machine-learning interatomic potential (MLIP[58–60]) models of FeRh for the FM and AF phases. The details of the simulations are described in Appendix C.

The resulting renormalized phonon band structures at room temperature are represented in Fig. 7. In the FM phase, all Fe atoms are equivalent by symmetry, so that the magnetic unit cell coincides with the B2 structure which can be used to compute phonon-related properties. This is not the case for the AF phase, where the spin up or down occupation of Fe atoms makes them inequivalent. Such a breaking of symmetry can have an important impact on the phonon properties[26]. To account for this effect, the phonons in the AF phase were computed using the magnetic unit cell.

For both phases, we find that the spectra are fully real, demonstrating their dynamical stability. Some previous works[22,24] had suggested the possibility of an additional low T phase for the AF phase, which our results do not support (at least down to 50 K).

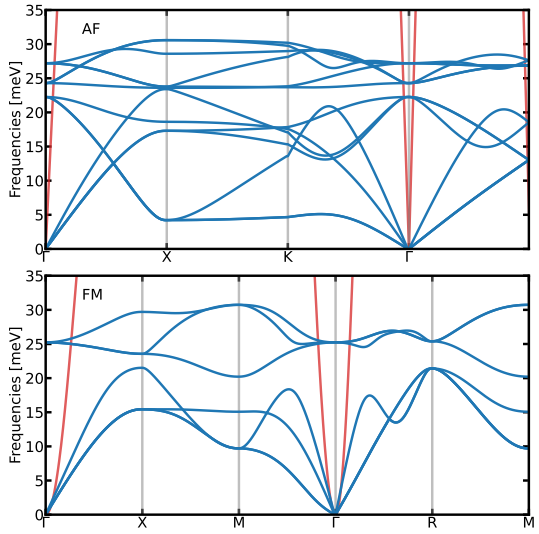

FIG. 7. Room temperature phonon band structure for (up) the AF and (down) the FM phase of FeRh. For comparison, the magnon band structures by Gu[61] are also shown in red (assuming no magnetic anisotropy). The phonons in the FM phase are computed using the B2 structure as the unit cell, while the magnetic unit cell was used for the AF phase.

With these phonons and the third order phonon scattering as input, we obtained the lattice thermal conductivity of the two phases using the iterative solution of the Boltzmann equation. Our results give $\kappa_{ph,\mathrm{AF}} = 11.84$ W m^{-1} K^{-1} $> \kappa_{ph,\mathrm{FM}} = 10.36$ W m^{-1} K^{-1} at room temperature. Our calculation differs from previous work in the literature[26], where the opposite trend was found. The thermal conductivities computed by Cazorla and Rurali[26] were based on the harmonic approximation at the ground-state volume and using a different exchange and correlation functional. We show in Appendix C that beyond the differences in the DFT calculations that are minor, the main difference in our results comes from the explicit variation of the interatomic force constants and volume with temperature. The difference in lattice κ_{ph} favors the AF phase, but only slightly. However, the experimentally observed asymmetry between FM and AF thermal conductivities also contains electronic and magnonic contributions to κ, which we proceed to estimate.

Electron thermal conductivity

The electronic thermal conductivity κ_e can be estimated from the charge conductivity σ, through the Wiedemann-Franz relationship. The latter is known not to hold universally, but breakdowns mainly appear for strongly correlated metals, strange band structures, or sub-micron structures[62]. In the present case if the Lorenz factor takes its ideal value of $L_0 = 2.44 \times 10^{-8}$ W.Ω.K^{-2}, we can extract the electron thermal conductivity as $\kappa_e = L_0 T \sigma$.

We measure the temperature-dependent resistance of a 195-nm-thick FeRh film which was grown together with the sample utilized for the thermoreflectance measurements above. The resistance measurement was carried out using the 4-point probe method by contacting the film with four pins arranged in a square 4 mm on each side. The temperature was controlled using a custom-made Peltier holder and no magnetic field was applied during the measurement. In this way we find at 360 K $1/\sigma_{\mathrm{AF}} = 1$ μΩ m and $1/\sigma_{\mathrm{FM}} = 0.6$ μΩ m, very close to values from the literature[63]. This implies $\kappa_{e,\mathrm{AF}} \approx 9$ W m^{-1} K^{-1} which is sensibly lower than $\kappa_{e,\mathrm{FM}} \approx 15$ W m^{-1} K^{-1}. Theoretical calculations of κ_e in FeRh based on its electronic band structure also show a slightly larger value for the FM phase: Jimenez *et al.*[25] find $\kappa_{e,\mathrm{AF}} \approx 21$ W m^{-1} K^{-1} and $\kappa_{e,\mathrm{FM}} \approx 27$ W m^{-1} K^{-1}, using a somewhat arbitrary temperature and energy independent relaxation time of 10^{-14} s. In their calculations the Lorenz factor is not presumed constant (and depends on the electronic band structure) but the κ_e is known only up to a rescaling by the relaxation time, which will be different for FM and AF phases, and should be energy/state dependent. Overall, we expect $\kappa_{e,\mathrm{FM}}$ to be a bit larger than $\kappa_{e,\mathrm{AF}}$, and of the order of 10–15 W m^{-1} K^{-1}.

Magnon thermal conductivity: model dispersion and lifetime

Finally, we wish to estimate the magnon contribution to the thermal conductivity. Wu *et al.*[29] calculate simultaneous lattice and spin dynamics for BCC Fe, and find that the magnon contribution to κ ($\kappa_m = 15$ W m^{-1} K^{-1}) is larger than the lattice one ($\kappa_{ph} = 8$ W m^{-1} K^{-1}), though they are skeptical of their κ_m. We have re-implemented the magnon band model from Gu and Antropov[61] as a python script, and added the calculation of the group velocities $v_{q\lambda}$ and a lifetime given by $1/\tau_{q\lambda} = \alpha_G \omega_{q\lambda}$ which depends only on the frequency of mode λ at wave vector q. Here α_G is the Gilbert damping parameter, which should vary with temperature and magnetic ordering (and in principle also with the magnon mode λ, q). Using these ingredients, one can calculate the thermal conductivity with a formula analogous to that for phonons (Eq. (11) in Appendix C):

$$\tilde{\kappa}_m^{ab}(\omega) = \frac{1}{V}\sum_{q\lambda} v_{q\lambda}^a v_{q\lambda}^b C_v(\omega_{q\lambda})\tau_{q\lambda}\,\delta(\omega-\omega_{q\lambda}) \quad (5)$$

$$\kappa_m^{ab} = \int \tilde{\kappa}_m^{ab}(\omega)d\omega \quad (6)$$

where a, b are Cartesian components, C_v is the mode specific heat ($[1/2x/(\sinh x/2)]^2$ with $x = \hbar\omega/k_BT$), and V is the unit cell volume. We call $\tilde{\kappa}$ the spectral thermal conductivity. The q integrations are carried out numerically on 100^3 point grids for the primitive cubic Brillouin Zone. In this framework, the band structure strongly favors $\kappa_{m,FM}$, through the much larger DOS at low frequency (quadratic vs linear dispersion), which boosts the C_v at low ω, where τ is also large. This effect is stronger than that of the magnon group velocities, which favor the AF phase (constant acoustic velocity), over the FM phase (zero velocity at Γ which grows linearly). The product $C_v\tau v^2$ yields $\tilde{\kappa}_{m,FM} \propto \omega^{1/2}$ for the FM phase, while $\tilde{\kappa}_{m,\mathrm{AF}} \propto \omega$. The Bose distribution weights most of C_v and κ_m at low frequencies, generically favoring $\kappa_{m,FM}$ over $\kappa_{m,AF}$.

An important ingredient of the calculation is the parameter α_G, in both phases. The only measurements of FeRh magnon damping have been performed in the uniform FM phase, for which quite a large spread has been reported. Intrinsic damping values of around 0.001–0.004 have been measured[64] or computed using a multiple scattering method including position and spin fluctuations[63]. Larger values between 0.03 and 0.1 have also been seen, and attributed to the spin-sink effect of either an adjacent Pt layer[65], or residual AF domains[66].

For the AF phase, a first principles calculation was made by Mahfouzi and Kioussis[67], and using their Eq. 5 we obtain values ranging from 0.03 to 0.3 between what they call low and high temperature. Simensen *et al.*[68] arrive at 0.3 with a magnon scattering theory.

Using a single conservative value $\alpha_G = 0.25$ for both phases, we obtain values of $\kappa_{m,\mathrm{AF}} \sim 15$ W m^{-1} K^{-1} and $\kappa_{m,\mathrm{FM}} \sim 90$ W m^{-1} K^{-1}. The former is reasonable, but the latter is too large compared to our measurements. Examining the different ingredients for our model, the magnon dispersion compares favorably with experiments[69] and the calculations of Sandratskii and Buczek[70], except for a small but crucial underestimation of the FM phase stiffness at low frequency and q, noted by Castets[69]. If the acoustic mode has a slight linear component (e.g. by mixing with phonon excitations) or much higher stiffness, the DOS, C_v and $\kappa_{m,\mathrm{FM}}$ will be strongly reduced. The main source of uncertainty is the simplistic lifetime model as $1/\omega\alpha_G$: the large DOS and lifetimes at low frequency give too much weight to the FM phase κ_m.

Estimate of the thermal resistance at the FeRh/MgO interface

The thermal interface resistance was estimated theoretically based on the bulk phonon dispersions of FeRh (FM and AFM) combined with those of MgO. The diffuse mismatch model (DMM) was used[71,72], which has two main hypotheses: (i) the phonons are transmitted based on their frequency matching and their group velocity component normal to the interface; (ii) detailed balance and a steady state is achieved, which allows to calculate the transmission probability. The implementation was carried out in the Abinit[73] package following the full phonon description in Ref.[74] and was benchmarked against their values for interfaces between Si, Cu and Al. For (100) oriented FeRh on (100) MgO[75] , the AFM phase has a room temperature interface resistance of 4.3 $\times 10^{-9}$ m^{2}K W^{-1}, and the FM phase of 4.2 $\times 10^{-9}$ m^{2}K W^{-1}. Other crystalline orientations tend to decrease the resistance, down to 2.3 (resp. 0.24) $\times 10^{-9}$ m^{2}K W^{-1} for FM (resp. AF) (111) FeRh on (111) MgO. The main factor boosting the interface resistance is the small overlap in frequency between light MgO and heavier FeRh. To fit the thermoreflectance spatial scans, we used the value $R_{th} = 4 \times 10^{-9}$ m^{2}K W^{-1}, but also considered the possibility of much larger values (see Fig. 4).

TABLE II. Numerical estimates of the different contributions to the thermal conductivity. The last column refers to the total value, to be compared to the experimentally measured one (Table I).

Phase	κ_{ph}	κ_e	κ_m	κ (W m^{-1} K^{-1})
AF	12	9	15	36
FM	10	15	90	115

DISCUSSION AND COMPARISON TO EXPERIMENTS

We find three comparable contributions for the thermal conductivity, between the lattice, electronic, and magnon terms (Table II). Each term has been estimated using available simulations or experimental input, and they are all on the order of 10 W m^{-1} K^{-1}, with $\kappa_{m,\mathrm{FM}}$ the only outlier. The sum renders quite nicely the measurements of $\kappa_{\mathrm{AF}} \sim 30$ W m^{-1} K^{-1}, but the lower measured κ_{FM} requires additional attention: the observed difference in the lattice κ_{ph} provides 1–2 W m^{-1} K^{-1}, but the other two terms favor FM over AF.

Several factors may contribute to lower κ_{FM}:

- the multi-domain state of the layer in its FM phase could give an extra contribution from ferromagnetic domain-wall resistance[76], but a large number of ferromagnetic domains is quite unlikely under the two-micron spot, due to the competition between exchange and magnetostatic energy cost.

- disorder will limit transport in both phases, but magnetic disorder (e.g., domains, impurities) will affect the FM phase transport more strongly as the dipolar interaction is longer ranged. The strong κ_m advantage of FM over AF for long wavelengths will be reduced by defects and grain boundaries.

- the low-q magnon phonon coupling is bound to play a critical role (see Fig. 7). Due to their quadratic dispersion and very similar frequencies, the FM magnons will interfere with acoustic phonons, limiting both lattice κ_{ph} and magnon κ_m. The impact of this coupling on the latter could have a significant impact on the total thermal conductivity on the FM phase. Compounding this effect, the AF magnon group velocity is much higher and there will be no coupling of magnons to acoustic phonons.

- Our model for magnon lifetimes is quite crude, and may break down. Beyond the temperature and magnetic state, the "true" $\alpha_{G,q\lambda} = 1/\omega_{q\lambda}\tau_{q\lambda}$ will also depend on the specific magnon mode. Any upper bound on the lifetimes at low q and low frequency will again reduce κ_{FM} more strongly.

CONCLUSIONS

Space and frequency-dependent thermoreflectance measurements were performed in order to determine the thermal conductivity of a 195-nm-thick FeRh film in a wide temperature range of 5 to 130°C, across the AF to FM transition. Unexpectedly (based on rough estimates made with the Wiedemann-Franz law), the thermal conductivity is found overall three times *larger* in the AF phase compared to the FM phase, a trend confirmed by the temporal decay of laser-pulsed generated incoherent phonons. These values were then used to estimate the expected transient and stationary temperature rises induced by a laser. To explain why the total FM thermal conductivity is lower than the AF one, we estimated the phononic contribution to κ from anharmonic first-principles dynamics, the electronic contribution from the experimental resistivity using Wiedemann-Franz, and the magnonic contribution using a linear spin wave model from the literature, with a Gilbert-type relaxation time. In the AF phase, the three components were found to be of the same order of magnitude, with a total of around 36 W m^{-1} K^{-1}, very close to the observed ≈ 30 W m^{-1} K^{-1}. In the FM phase, however, the calculated thermal conductivity rockets to ≈ 115 W m^{-1} K^{-1}, which is unrealistically large with regards to the observed ≈ 10 W m^{-1} K^{-1}. More accurate modelling of electronic and magnonic contributions will be required: in particular the large uncertainties in the magnetic damping, the magnon-phonon coupling, and the effects of disorder lead to a strong overestimate of all three components of κ.

These results underscore the complexity of FeRh and the importance of the three-way couplings between electrons, phonons, and magnons, which are on equal footing in the total thermal conductivity.

ACKNOWLEDGMENTS

This work has been partly supported by the French Agence Nationale de la Recherche (ANR ACAF 20-CE30-0027). We acknowledge M. Vabre (Institut des Nanosciences de Paris) for technical assistance. Access to the CEITEC Nano Research Infrastructure was supported by the Ministry of Education, Youth and Sports (MEYS) of the Czech Republic under the project CzechNanoLab (LM2023051). AC and MJV acknowledge the Fonds de la Recherche Scientifique (FRS-FNRS Belgium) for PdR Grant No. T.0103.19 - ALPS, and ARC project DREAMS (G.A. 21/25-11) funded by Federation Wallonie Bruxelles and ULiege, and the Excellence of Science (EOS) program (grant 40007563-CONNECT) funded by the FWO and F.R.S.-FNRS. Simulation time was awarded by the Belgian share of EuroHPC in LUMI hosted by CSC in Finland, by the CECI (FRS-FNRS Belgium Grant No. 2.5020.11), as well as the Zenobe Tier-1 of the Fédération Wallonie-Bruxelles (Walloon Region grant agreement No. 1117545).

APPENDIX A: PARAMETERS

The values for the thermal conductivity $\kappa_0(T)$, diffusivity $D_0(T)$ and specific heat $C_0(T)$ of MgO were taken from

Ref. 77. The specific heat $C_1(T)$ of FeRh was found in Ref. 1, where they measured much thicker, polycristalline films. We believe any error on this parameter should impact only mildly the determination of κ_1. Indeed this parameter intervenes through the calculation of the diffusivity of FeRh, $D_1(T)$, which has a minor effect on the analysis of modulated thermoreflectance experiments in the "insulating-over-conductive layer" configuration[30]. The volume density of FeRh was taken phase-dependent and temperature-independent[78] from Ref. 22: $\rho_{1,\mathrm{AF}} = 9744.51$ kg m^{-3} and $\rho_{1,\mathrm{FM}} = 9590.11$ kg m^{-3}. A standard knife-edge measurement in our experimental geometry gives d_{pump}=2.$\pm$0.1μm. The reflectance of FeRh was taken phase-dependent and estimated as: $R_{\mathrm{AF}} = 0.75$ and $R_{\mathrm{FM}} = 0.72$ by comparing to the reflectance of Aluminium. Finally, the light absorption coefficient of FeRh was estimated in both phases by measuring the light reflected from/transmitted through a 30 nm sample grown in similar conditions. It corresponds to a penetration depth of around 10 nm (resp. 12-13 nm) at 532 nm (resp. 773 nm), much less than the thickness of the film $h = 195$ nm.

APPENDIX B: DETAILS ON THE PICOSECOND ACOUSTICS EXPERIMENTS AND MODELLING

The picosecond acoustics pump-probe set-up is described in Peronne *et al.*[45]. More specifically to these measurements, the laser repetition rate was 80 MHz, with a modulation of 1 MHz. Its wavelength was 773 nm, and the beam diameter was of the order of $\approx 15\ \mu m$. The power of the pump beam was around P=32 mW, that of the probe around 4 mW. The delay line was scanned mechanically at 40 nm/ps. The model is based on the 1D heat diffusion equation and the propagation equation for elastic waves. Given the short time scale (300 ps), the FeRh layer can be considered as a semi-infinite medium since the thermal wave has not reached the substrate. The surface displacement $u(t,z=0)$, propagating strain $S_{prop}(t,z)$ and temperature increase $\Delta T(t,z)$ are obtained as[79]:

$$u(0,t) = -\frac{S_0}{\alpha}\left(1-\frac{x\exp(-\omega_\alpha t)}{x+1}-\frac{x\exp(\omega_D t)}{x^2-1}\mathrm{Erfc}\left(\sqrt{\omega_D t}\right)+\frac{\exp(x\omega_\alpha t)}{x^2-1}\mathrm{Erfc}\left(\sqrt{x\omega_\alpha t}\right)\right) \quad (7)$$

$$S_{prop} = \begin{cases} z-vt>0 & \frac{S_0}{1-x^2}\left(\exp(-\omega_D(z/v-t))-x\exp(-\omega_\alpha(z/v-t))\right) \\ z-vt<0 & \frac{S_0}{1-x^2}\left(\exp(\omega_D(t-z/v))\mathrm{Erfc}\left(\sqrt{\omega_D(t-z/v)}\right)-x\exp(x\omega_\alpha(t-z/v))\mathrm{Erfc}\left(\sqrt{x\omega_\alpha(t-z/v)}\right)\right) \end{cases} \quad (8)$$

$$\Delta T(t,z) = \frac{F(1-R)\alpha}{2\rho_1 C_1}\exp(\omega_D t)\left(\exp(-\alpha z)\mathrm{Erfc}\left(\frac{-z+2D_1\alpha t}{2\sqrt{D_1 t}}\right)+\exp(\alpha z)\mathrm{Erfc}\left(\frac{z+2D_1\alpha t}{2\sqrt{D_1 t}}\right)\right), \quad (9)$$

where α, D_1, v, ρ_1, C_1, R, are the absorption coefficient, diffusivity, longitudinal acoustic velocity, specific heat, and reflectivity coefficient of FeRh, respectively. We take $\kappa_{AF}(\kappa_{FM})$=30(10) W m^{-1} K^{-1}, hence $D_{AF}(D_{FM}) = 9.3(2.7)\times10^{-6}$ m^2 s^{-1}, and $v_{AF}(v_{FM})$ =4741 (4865) m s^{-1}[80]. F=0.2 mJ cm^{-2} is the laser fluence. We note $\omega_\alpha = \alpha v$, $\omega_D = D_1\alpha^2$, $x = \omega_\alpha/\omega_D$. The real and imaginary parts of the refractive index $n = n' + jn''$ were obtained at λ =773 nm as a function of temperature by ellipsometry from 20°C to 120°C. For instance at 25°C for the AF phase and 120°C for the FM phase: $n'_{AF}(n'_{FM})$ =4.1(4.2), $n''_{AF}(n''_{FM})$ =5(4.4) and hence $\alpha_{AF}(\alpha_{FM})$=8.1(7.2)$\times10^7$ m^{-1}. The derivatives are $dn'_{AF}/dT(dn'_{FM}/dT) = 7.6(6.8)\times10^{-3}$ and $dn''_{AF}/dT(dn''_{FM}/dT) = 4(2.8)\times10^{-3}$. S_0 is defined as $3\beta B\alpha(1-R)F/\left(\rho_1^2 C_1 v^2\right)$ where β is the thermal expansion coefficient, and B the bulk modulus. Using data from[19,80] we have $S_{0AF}(S_{0FM}) = 3.8(2)\times10^{-4}$. The derivative dn/dS is not known but taking a large value of 30 consistent with data from the literature[81], we get a smaller contribution of the propagating strain in the interferometric signal.

APPENDIX C: METHOD AND COMPUTATIONAL DETAILS FOR LATTICE THERMAL CONDUCTIVITY

Temperature dependent effective potential

The temperature dependent effective potential[52,56,57] method is based on the construction of an effective anharmonic Hamiltonian of the form

$$H = \sum_i \frac{p_i^2}{2M_i} + \frac{1}{2}\sum_{ij}\sum_{ab}\Theta_{ij}^{ab}u_i^a u_j^b + \frac{1}{3!}\sum_{ijk}\sum_{abc}\Psi_{ijk}^{abc}u_i^a u_j^b u_k^c \quad (10)$$

where u_i^a and p_i are respectively the displacement along the cartesian direction a and momentum of atom i with mass M_i, and Θ_{ij}^{ab} and Ψ_{ijk}^{abc} are the second and third order interatomic force constants, which we fit to molecular dynamics data using ordinary least-squares methods. The effectiveness of this Hamiltonian comes from the iterative nature of the fit, where each order is fit on the residual of the previous order. While this procedure ensures that the lowest orders intrinsically include most of the anharmonicity, it also produces, as the name suggests, a temperature-dependent effective potential, so that individual MD simulations have to be run for each temperature of interest.

Once the interatomic force constants are extracted from

MD simulations, the thermal conductivity can be computed using the Boltzmann equation. In this work, the solution of this equation was obtained with an iterative algorithm[50], after which the thermal conductivity tensor is written as

$$\kappa_{ph}^{ab} = \frac{1}{V}\sum_{\lambda} c_\lambda v_\lambda^a F_\lambda^b \tag{11}$$

with V the volume of the unit cell, c_λ the heat capacity associated with mode λ, v_λ^a the group velocity of mode λ along cartesian direction a, and F_λ^a is the non-equilibrium phonon distribution accounting for the phonon relaxation, for which the BTE must be solved self-consistently. The Boltzmann equation was solved on a $25\times25\times25$ **q**-point grid and using an adaptive gaussian scheme for the Dirac delta[82].

For both the extraction of the interatomic force constants and the computation of the thermal conductivity, we used the implementation provided by the TDEP package[83].

Machine-learning interatomic potential and Molecular dynamics

To decrease the important computational cost associated with the MD simulations, we used two machine-learning interatomic potential (MLIP) within the Moment Tensor Potential[59] formalism, one for the AF phase and the other one for the FM phase. The MLIP were fit on DFT calculations performed with the Abinit suite[73] using the PBE parameterization of the exchange and correlation functional[84] in the PAW formalism[85,86]. These MLIP were successfully used to study the elastic properties of FeRh and we refer to our previous work[80] for more details about the parameters and dataset used in their construction.

With the MLIP, we compute the effective anharmonic Hamiltonian from 100 to 500 K in steps of 100 K. For each temperature, we run two 100 ps MD simulations on $8\times8\times8$ supercells, with a time step of 1 fs using the LAMMPS package[87]. The first MD run is performed in the NPT ensemble, and is used to compute the average equilibrium volume, while the second one employs this equilibrium volume in the NVT ensemble, in order to compute the renormalized interatomic force constants. These force constants are computed using 900 uncorrelated configurations, extracted from the NVT MD trajectory after 10 ps of equilibration.

Temperature dependent phonons

The temperature dependent phonon dispersions of both phases are plotted on Fig. 8. For the FM phase, we observe only a slight softening of the phonon frequencies with an increase in temperature, indicating a relatively small anharmonicity in the system even at a temperature of 500 K. It should be noted that most of this temperature dependence can be attributed to the thermal expansion. While most of the modes in the AF phase show similar behavior, this is not the case for the lowest energy mode located at the high symmetry X point. This mode, which we find to be imaginary in the harmonic approximation (as in previous literature, e.g.,[22,53–55]) has instead the opposite trend: a strong hardening with temperature. We note that even at 100 K, which is the lowest temperature studied here, this mode and the whole spectrum are fully real, demonstrating the stability of the AF phase.

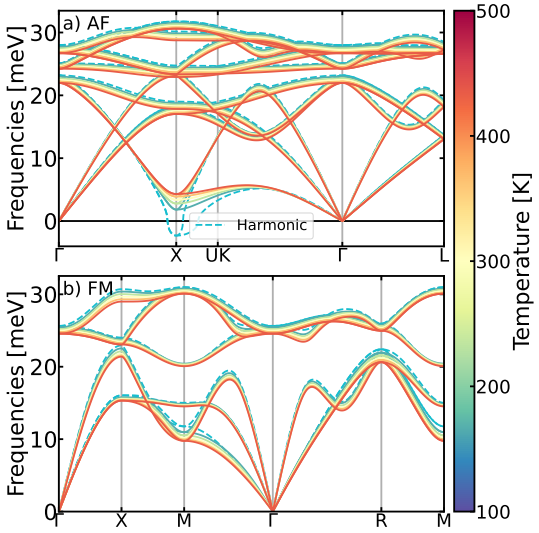

FIG. 8. Temperature dependent phonons for a) the FM and b) the AF phase of FeRh. In b) the harmonic phonons computed with finite difference to highlight the stabilization of the system by anharmonicity. The phonons in the FM phase are computed using the B2 structure as the unit cell, while the magnetic unit cell was used for the AF phase.

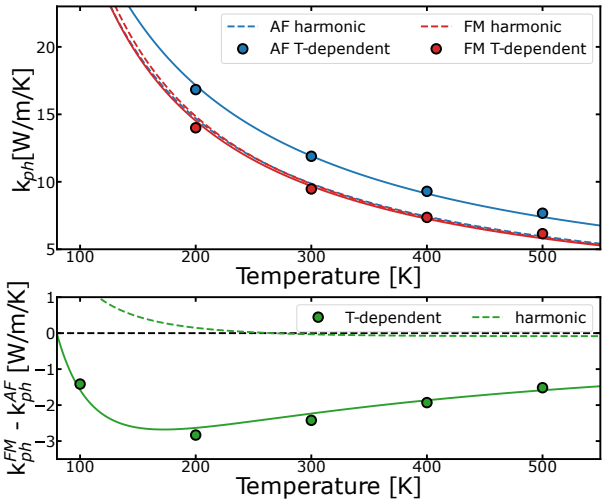

FIG. 9. a) Theoretical lattice thermal conductivity of FeRh computed for the AF phase, in blue, and the FM phase, in red. The harmonic results, represented with dashed lines, are obtained with IFC computed at $T = 25$ K. b) Difference of thermal conductivity between the FM and the AF phases.

Using these force constants as input, we computed the thermal conductivity by solving the iterative Boltzmann equation for each temperature. Our results, Fig. 9, show a slightly

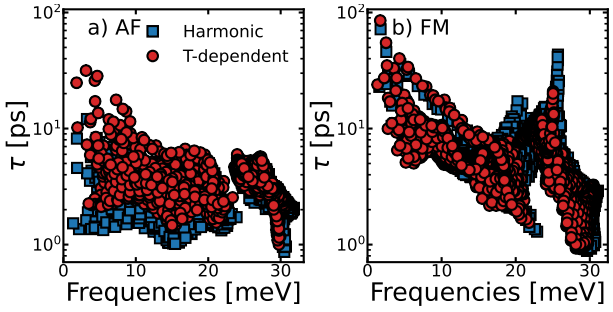

FIG. 10. Phonon lifetimes at 300 K in a) the AF phase and b) the FM phase. In both figures, the harmonic results are taken without accounting for the temperature dependence of the phonons.

larger κ_{ph} for the AF phase than for the FM phase above 150 K. As already stated in the main text, these finding differs from the results of Cazorla and Rurali[26], where the opposite trend was found based on the harmonic approximation at the 0K relaxed volume. To better understand the origin of this discrepancy, we computed the thermal conductivities with our MLIP using analogous approximations. Due to the imaginary mode in the AF phase, and in order to provide a meaningful comparison, we used IFC computed at a temperature of 25 K and at the reference relaxed volume for both phases, instead of the harmonic ones. As shown in Fig. 9, these approximations yield the same trend as in Ref. 26, with $\kappa_{ph,\mathrm{FM}} > \kappa_{ph,\mathrm{AF}}$ for all temperatures. To explain the opposite trend obtained with fully anharmonic IFC, we compare the $T = 300$ K phonon lifetimes obtained with the two approaches in Fig. 10.

The FM phase presents only a slight evolution of the lifetimes, confirming the low anharmonicity of this phase. On the contrary, the renormalization of the IFC brings an important *increase* of the phonon lifetimes in the AF phase. This counter-intuitive effect can be understood as the decrease of the scattering phase space due to the renormalization of the phonons[88]. In the AF phase of FeRh, this effect is sufficiently strong for $\kappa_{ph,\mathrm{AF}}$ to exceed $\kappa_{ph,\mathrm{FM}}$.

[1] M. Richardson, D. Melville, and J. A. Ricodeau, Physics Letters A **46**, 153 (1973).
[2] M. P. Annaorazov, K. A. Asatryan, G. Myalikgulyev, S. A. Nikitin, A. M. Tishin, and A. L. Tyurin, Cryogenics **32**, 867 (1992).
[3] X. Marti, I. Fina, C. Frontera, J. Liu, P. Wadley, Q. He, R. J. Paull, J. D. Clarkson, J. Kudrnovský, I. Turek, J. Kuneš, D. Yi, J.-H. Chu, C. T. Nelson, L. You, E. Arenholz, S. Salahuddin, J. Fontcuberta, T. Jungwirth, and R. Ramesh, Nature Materials **13**, 367 (2014), arXiv:0402594v3 [arXiv:cond-mat].
[4] J.-U. Thiele, S. Maat, and E. E. Fullerton, Applied Physics Letters **82**, 2859 (2003).
[5] S. Cervera, M. Trassinelli, M. Marangolo, C. Carrétéro, V. Garcia, S. Hidki, E. Jacquet, E. Lamour, A. Lévy, S. Macé, C. Prigent, J. P. Rozet, S. Steydli, and D. Vernhet, Physical Review Materials **1**, 065402 (2017).
[6] J.-U. Thiele, M. Buess, and C. H. Back, Applied Physics Letters **85**, 2857 (2004).
[7] G. Ju, J. Hohlfeld, B. Bergman, R. J. M. van de Veerdonk, O. N. Mryasov, J.-Y. Kim, X. Wu, D. Weller, and B. Koopmans, Physical Review Letters **93**, 197403 (2004).
[8] B. Bergman, G. Ju, J. Hohlfeld, R. J. M. van de Veerdonk, J.-Y. Kim, X. Wu, D. Weller, and B. Koopmans, Physical Review B **73**, 060407 (2006).
[9] I. Radu, C. Stamm, N. Pontius, T. Kachel, P. Ramm, J.-U. Thiele, H. A. Dürr, and C. H. Back, Physical Review B **81**, 104415 (2010).
[10] F. Quirin, M. Vattilana, U. Shymanovich, A.-E. El-Kamhawy, A. Tarasevitch, J. Hohlfeld, D. von der Linde, and K. Sokolowski-Tinten, Physical Review B **85**, 020103(R) (2012).
[11] S. O. Mariager, F. Pressacco, G. Ingold, A. Caviezel, E. Möhr-Vorobeva, P. Beaud, S. L. Johnson, C. J. Milne, E. Mancini, S. Moyerman, E. E. Fullerton, R. Feidenhans'l, C. H. Back, and C. Quitmann, Physical Review Letters **108**, 087201 (2012).
[12] F. Pressacco, D. Sangalli, V. Uhlíř, D. Kutnyakhov, J. A. Arregi, S. Y. Agustsson, G. Brenner, H. Redlin, M. Heber, D. Vasilyev, J. Demsar, G. Schönhense, M. Gatti, A. Marini, W. Wurth, and F. Sirotti, Nature Communications **12**, 5088 (2021), arXiv:2102.09265.
[13] A. B. Mei, I. Gray, Y. Tang, J. Schubert, D. Werder, J. Bartell, D. C. Ralph, G. D. Fuchs, and D. G. Schlom, Advanced Materials **32**, 2001080 (2020).
[14] G. Li, R. Medapalli, J. H. Mentink, R. V. Mikhaylovskiy, T. G. H. Blank, S. K. K. Patel, A. K. Zvezdin, T. Rasing, E. E. Fullerton, and A. V. Kimel, Nature Communications **13**, 2998 (2022).
[15] J. A. Arregi, O. Caha, and V. Uhlíř, Physical Review B **101**, 174413 (2020).
[16] D. W. Cooke, F. Hellman, C. Baldasseroni, C. Bordel, S. Moyerman, and E. E. Fullerton, Physical Review Letters **109**, 255901 (2012).
[17] S. Shihab, L. Thevenard, A. Lemaître, J. Y. Duquesne, and C. Gourdon, Journal of Applied Physics **119**, 153904 (2016).
[18] F. Pressacco, V. Uhlíř, M. Gatti, A. Nicolaou, A. Bendounan, J. A. Arregi, S. K. K. Patel, E. E. Fullerton, D. Krizmancic, and F. Sirotti, Structural Dynamics **5**, 034501 (2018).
[19] Y. Ahn, J. Zhang, Z. Chu, D. A. Walko, S. O. Hruszkewycz, E. E. Fullerton, P. G. Evans, and H. Wen, ACS Nano **17**, 18843 (2023).
[20] T. Moriyama, N. Matsuzaki, K.-J. Kim, I. Suzuki, T. Taniyama, and T. Ono, Applied Physics Letters **107**, 122403 (2015).
[21] B. Fogarassy, T. Kemény, L. Pál, and J. Tóth, Physical Review Letters **29**, 288 (1972).
[22] U. Aschauer, R. Braddell, S. A. Brechbühl, P. M. Derlet, and N. A. Spaldin, Physical Review B **94**, 014109 (2016), arXiv:1603.01827.
[23] W. He, H. Huang, and X. Ma, Materials Letters **195**, 156 (2017).
[24] M. Wolloch, M. E. Gruner, W. Keune, P. Mohn, J. Redinger, F. Hofer, D. Suess, R. Podloucky, J. Landers, S. Salamon, F. Scheibel, D. Spoddig, R. Witte, B. Roldan Cuenya, O. Gutfleisch, M. Y. Hu, J. Zhao, T. Toellner, E. E. Alp, M. Siewert, P. Entel, R. Pentcheva, and H. Wende, Physical Review B **94**, 174435 (2016).
[25] M. J. Jiménez, A. B. Schvval, and G. F. Cabeza, Computational Materials Science **172**, 109385 (2020).
[26] C. Cazorla and R. Rurali, Physical Review B **105**, 104401 (2022).
[27] Y. Hao, L. Zhang, and J. Zhu, Zeitschrift für Naturforschung A **75**, 789 (2020).

[28] V. Uhlíř, J. A. Arregi, and E. E. Fullerton, Nature Communications **7**, 13113 (2016), arXiv:1605.06823.

[29] X. Wu, Z. Liu, and T. Luo, Journal of Applied Physics **123**, 085109 (2018), arXiv:1712.09002.

[30] D. Fournier, M. Marangolo, and C. Frétigny, Journal of Applied Physics **128**, 241101 (2020).

[31] M. Rahimi, K. Sobnath, F. Mallet, P. Lafarge, C. Barraud, W. Daney De Marcillac, D. Fournier, and M. L. Della Rocca, Physical Review Applied **19**, 1 (2023).

[32] C. Frétigny, J. P. Roger, V. Reita, and D. Fournier, Journal of Applied Physics **102**, 116104 (2007).

[33] X. Qian, Z. Ding, J. Shin, A. J. Schmidt, and G. Chen, Review of Scientific Instruments **91** (2020), 10.1063/5.0003770.

[34] V. Saidl, M. Brajer, L. Horák, H. Reichlová, K. Výborný, M. Veis, T. Janda, F. Trojánek, M. Maryško, I. Fina, X. Marti, T. Jungwirth, and P. Němec, New Journal of Physics **18**, 083017 (2016).

[35] S. P. Bennett, M. Currie, O. M. J. van 't Erve, and I. I. Mazin, Optical Materials Express **9**, 2870 (2019).

[36] J. A. Arregi, F. Ringe, J. Hajduček, O. Gomonay, T. Molnár, J. Jaskowiec, and V. Uhlíř, Journal of Physics: Materials **6**, 034003 (2023).

[37] A. Rosencwaig and A. Gersho, Journal of Applied Physics **47**, 64 (1976).

[38] With α tending to infinity, one recovers the usual expression used in thermoreflectance microscopy (Eq. (10) of Ref. 30). Ignoring the absorption of the pump beam leads to an overestimate of the thermal conductivity of about 5% when analyzing our data.

[39] C. Frétigny, J.-Y. Duquesne, D. Fournier, and F. Xu, Journal of Applied Physics **111**, 084313 (2012).

[40] Y. Xian, P. Zhang, S. Zhai, P. Yuan, and D. Yang, Applied Thermal Engineering **130**, 1530 (2018).

[41] J.-Y. Duquesne, Physical Review B **79**, 153304 (2009).

[42] H.-K. Lyeo and D. G. Cahill, Physical Review B **73**, 144301 (2006).

[43] J. Zhu, D. Tang, W. Wang, J. Liu, K. W. Holub, and R. Yang, Journal of Applied Physics **108** (2010), 10.1063/1.3504213.

[44] C. Frétigny, J. Y. Duquesne, and D. Fournier, International Journal of Thermophysics **36**, 1281 (2015).

[45] E. Péronne, N. Chuecos, L. Thevenard, and B. Perrin, Physical Review B **95**, 064306 (2017).

[46] In that case, the transient out-of-plane strain induced by a pulsed laser is measured using time-resolved X-ray diffraction. κ_{FeRh} and R_{th} are obtained simultaneously by fitting the time-dependent thickness-averaged strain variations using a layer-resolved 1D thermal transport model, and a DC measurement of the linear thermal expansion.

[47] Y. S. Touloukian, *Thermophysical Properties of Matter: Thermal Diffusivity* (Plenum Press, 1973).

[48] K.-W. Kim, H. W. Lee, K. J. Lee, and M. D. Stiles, Physical Review Letters **111**, 1 (2013), arXiv:1308.1198.

[49] G. K. White and S. B. Woods, Canadian Journal of Physics **35**, 248 (1957).

[50] M. Omini and A. Sparavigna, Physica B: Condensed Matter **212**, 101 (1995).

[51] A. J. H. McGaughey, A. Jain, H.-Y. Kim, and B. Fu, Journal of Applied Physics **125**, 011101 (2019).

[52] O. Hellman and D. A. Broido, Physical Review B **90**, 134309 (2014).

[53] J. Kim, R. Ramesh, and N. Kioussis, Physical Review B **94**, 180407(R) (2016).

[54] N. A. Zarkevich and D. D. Johnson, Physical Review B **97**, 014202 (2018), arXiv:1710.04199.

[55] M. P. Belov, A. B. Syzdykova, and I. A. Abrikosov, Physical Review B **101**, 134303 (2020).

[56] O. Hellman, I. A. Abrikosov, and S. I. Simak, Physical Review B **84**, 180301 (2011).

[57] O. Hellman and I. A. Abrikosov, Physical Review B **88**, 144301 (2013).

[58] I. S. Novikov, K. Gubaev, E. V. Podryabinkin, and A. V. Shapeev, Machine Learning: Science and Technology **2**, 025002 (2021).

[59] A. V. Shapeev, Multiscale Modeling & Simulation **14**, 1153–1173 (2016).

[60] Y. Zuo, C. Chen, X. Li, Z. Deng, Y. Chen, J. Behler, G. Csányi, A. V. Shapeev, A. P. Thompson, M. A. Wood, and S. P. Ong, J. Phys. Chem. A **124**, 731 (2020).

[61] R. Y. Gu and V. P. Antropov, Physical Review B **72**, 012403 (2005).

[62] B. Zink, A. Avery, R. Sultan, D. Bassett, and M. Pufall, Solid State Communications **150**, 514 (2010).

[63] S. Mankovsky, S. Polesya, K. Chadova, H. Ebert, J. B. Staunton, T. Gruenbaum, M. A. W. Schoen, C. H. Back, X. Z. Chen, and C. Song, Physical Review B **95**, 155139 (2017).

[64] E. Mancini, F. Pressacco, M. Haertinger, E. E. Fullerton, T. Suzuki, G. Woltersdorf, and C. H. Back, Journal of Physics D: Applied Physics **46**, 245302 (2013).

[65] K. Tanaka, T. Moriyama, T. Usami, T. Taniyama, and T. Ono, Applied Physics Express **11**, 013008 (2017).

[66] T. Usami, M. Itoh, and T. Taniyama, AIP Advances **11**, 045302 (2021).

[67] F. Mahfouzi and N. Kioussis, Physical Review B **98**, 220410(R) (2018).

[68] H. T. Simensen, A. Kamra, R. E. Troncoso, and A. Brataas, Physical Review B **101**, 020403 (2020).

[69] A. Castets, D. Tochetti, and B. Hennion, Physica B+C **86-88**, 353 (1977).

[70] L. M. Sandratskii and P. Buczek, Physical Review B - Condensed Matter and Materials Physics **85**, 1 (2012).

[71] E. T. Swartz and R. O. Pohl, Appl. Phys. Lett. **51**, 200 (1987).

[72] E. T. Swartz and R. O. Pohl, Rev. Mod. Phys. **61**, 605 (1989).

[73] X. Gonze, B. Amadon, G. Antonius, F. Arnardi, L. Baguet, J.-M. Beuken, J. Bieder, F. Bottin, J. Bouchet, E. Bousquet, N. Brouwer, F. Bruneval, G. Brunin, T. Cavignac, J.-B. Charraud, W. Chen, M. Côté, S. Cottenier, J. Denier, G. Geneste, P. Ghosez, M. Giantomassi, Y. Gillet, O. Gingras, D. R. Hamann, G. Hautier, X. He, N. Helbig, N. Holzwarth, Y. Jia, F. Jollet, W. Lafargue-Dit-Hauret, K. Lejaeghere, M. A. Marques, A. Martin, C. Martins, H. P. Miranda, F. Naccarato, K. Persson, G. Petretto, V. Planes, Y. Pouillon, S. Prokhorenko, F. Ricci, G.-M. Rignanese, A. H. Romero, M. M. Schmitt, M. Torrent, M. J. van Setten, B. V. Troeye, M. J. Verstraete, G. Zérah, and J. W. Zwanziger, Computer Physics Communications **248**, 107042 (2020).

[74] P. Reddy, K. Castelino, and A. Majumdar, Applied Physics Letters **87**, 211908 (2005).

[75] Note that in the DMM, the orientation around the axis normal (rotation of FeRh by 45° in our case) is not taken into account.

[76] H. T. Huang, M. F. Lai, Y. F. Hou, and Z. H. Wei, Nano Letters **15**, 2773 (2015).

[77] A. M. Hofmeister, Physics and Chemistry of Minerals **41**, 361 (2014).

[78] This is a decent approximation given the weak temperature-dependence of a measured experimentally by Arregi *et al.*[15].

[79] B. Perrin, *Microscale and Nanoscale Heat Transfer*, edited by S. Volz, Topics in Applied Physics, Vol. 107 (Springer Berlin Heidelberg, 2007).

[80] D. Ourdani, A. Castellano, A. K. Vythelingum, J. A. Arregi, V. Uhlíř, B. Perrin, M. Belmeguenai, Y. Roussigné, C. Gourdon, M. J. Verstraete, and L. Thevenard, "hal-04526444," (2024), preprint.

[81] D. Royer and E. Dieulesaint, *Elastic Waves in Solids I: Free and Guided Propagation*, Advanced Texts in Physics (Springer, 2000).
[82] J. R. Yates, X. Wang, D. Vanderbilt, and I. Souza, Physical Review B. **75**, 195121 (2007).
[83] F. Knoop, N. Shulumba, A. Castellano, J. P. A. Batista, R. Farris, M. J. Verstraete, M. Heine, D. Broido, D. S. Kim, J. Klarbring, I. A. Abrikosov, S. I. Simak, and O. Hellman, Journal of Open Source Software **9**, 6150 (2024).
[84] J. P. Perdew, K. Burke, and M. Ernzerhof, Physical Review Letters **77**, 3865 (1996).
[85] P. E. Blöchl, Physical Review B **50**, 17953 (1994).
[86] F. Jollet, M. Torrent, and N. Holzwarth, Computer Physics Communications **185**, 1246 (2014).
[87] A. P. Thompson, H. M. Aktulga, R. Berger, D. S. Bolintineanu, W. M. Brown, P. S. Crozier, P. J. in 't Veld, A. Kohlmeyer, S. G. Moore, T. D. Nguyen, R. Shan, M. J. Stevens, J. Tranchida, C. Trott, and S. J. Plimpton, Computer Physics Communications **271**, 108171 (2022).
[88] Y. Yang, L. Zhao, D. Yi, T. Xu, Y. Chai, C. Zhang, D. Jiang, Y. Ji, W. Jiang, J. Tang, P. Yu, H. Wu, and T. Nan, (2022), arXiv:2212.04049.